

Supplementary Materials for
A 3D biomimetic optoelectronic scaffold repairs cranial defects

Huachun Wang *et al.*

Corresponding author: Yuguang Wang, wangyuguang@bjmu.edu.cn; Xing Sheng, xingsheng@tsinghua.edu.cn

Sci. Adv. **9**, eabq7750 (2023)
DOI: 10.1126/sciadv.abq7750

This PDF file includes:

Figs. S1 to S18

Fig. S1.

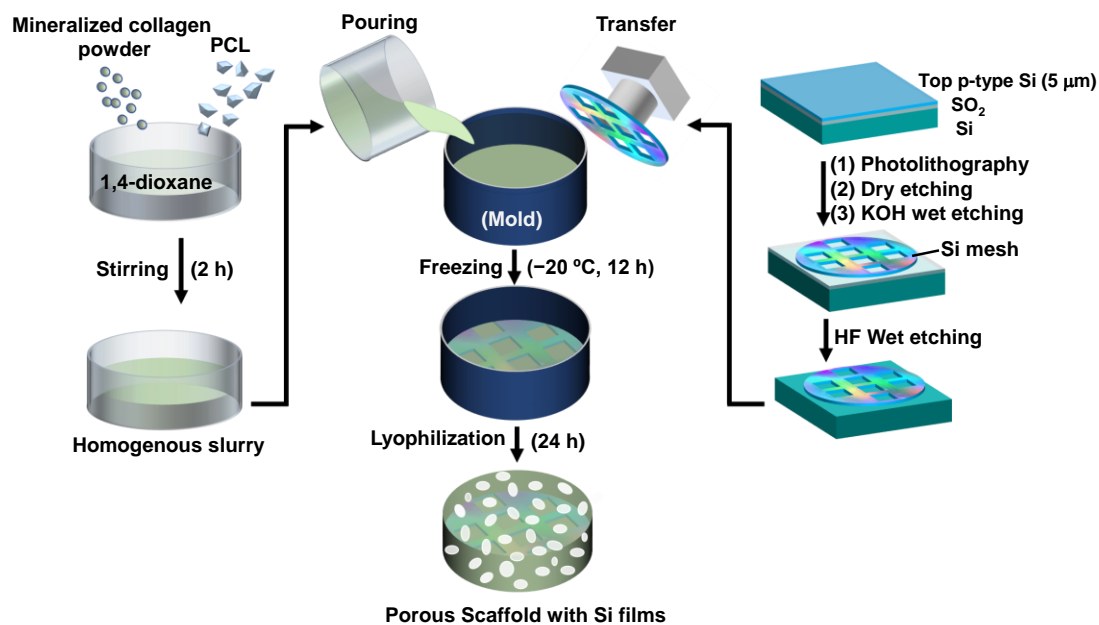


Fig. S1. Schematic illustration of processing flow for the fabrication of Si based 3D optoelectronic scaffold.

Fig. S2.

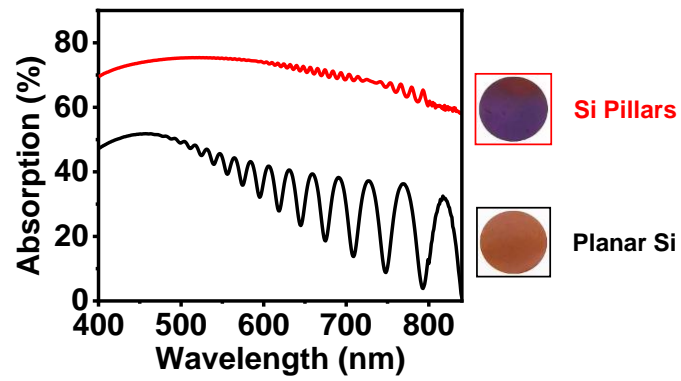


Fig. S2. Optical images and corresponding absorption spectra for Si pillars and planar Si samples.

Fig. S3.

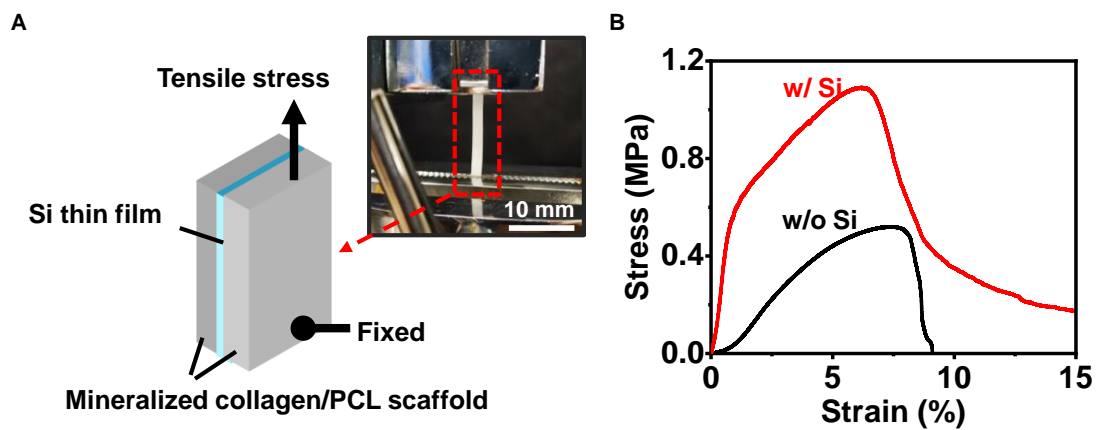


Fig. S3. Mechanical characterization of scaffolds. (A) Schematic illustration and optical image for the mechanical testing setup. (B) Measured strain-stress curves for 3D scaffolds with and without embedded Si films.

Fig. S4.

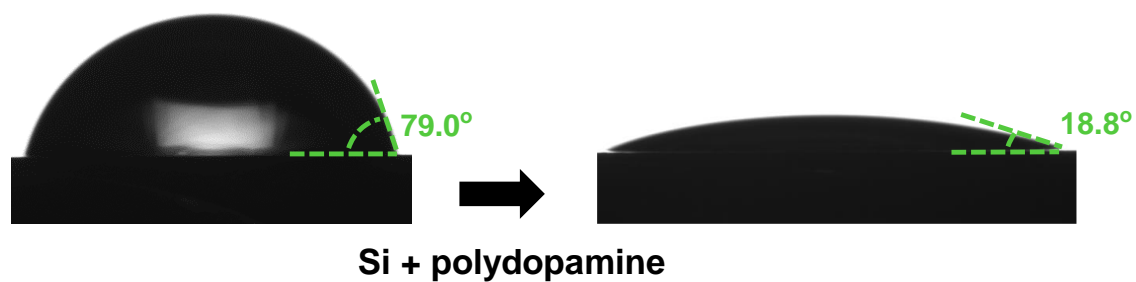


Fig. S4. Wetting properties of Si surfaces. Photographs showing contact angles for water droplets on Si surfaces before (left) and after (right) polydopamine coating for 30 min.

Fig. S5.

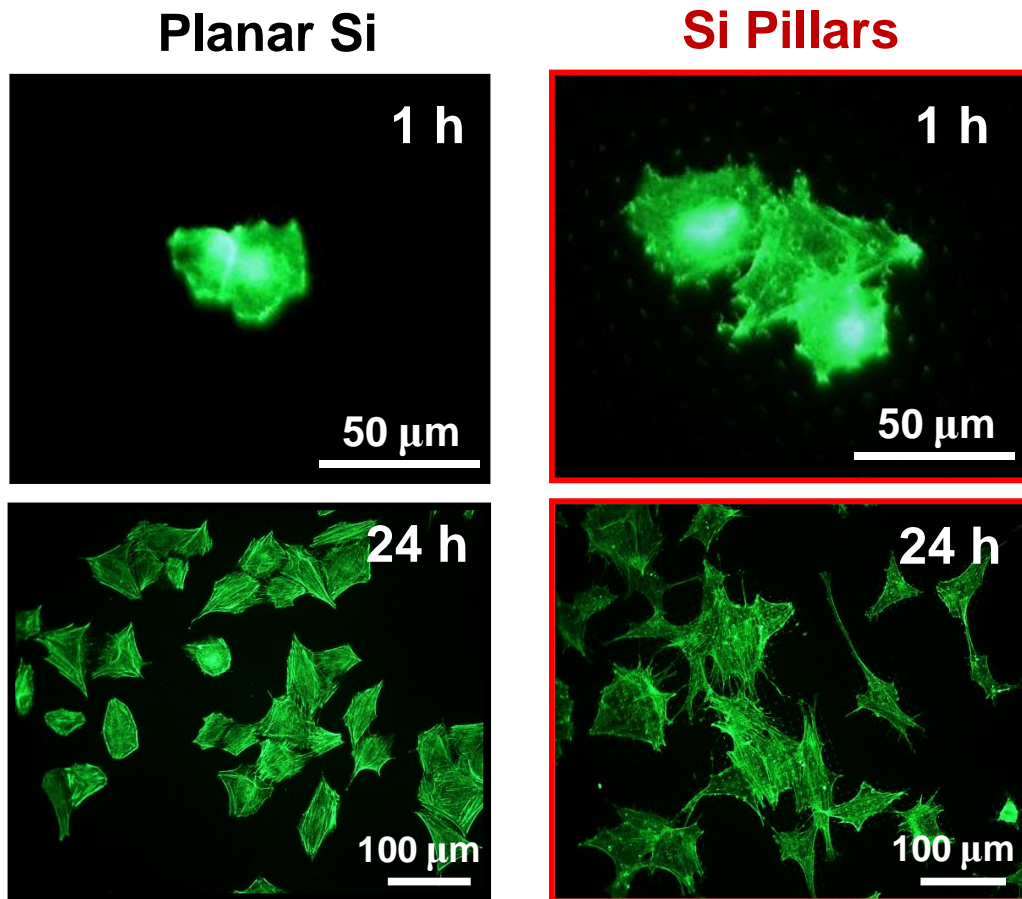


Fig. S5. Fluorescent images of MC3T3-E1 cells. These cells are cultured on planar Si (left) and Si pillars (right) after seeded for 1 h and 24 h, green: actin cytoskeleton.

Fig. S6.

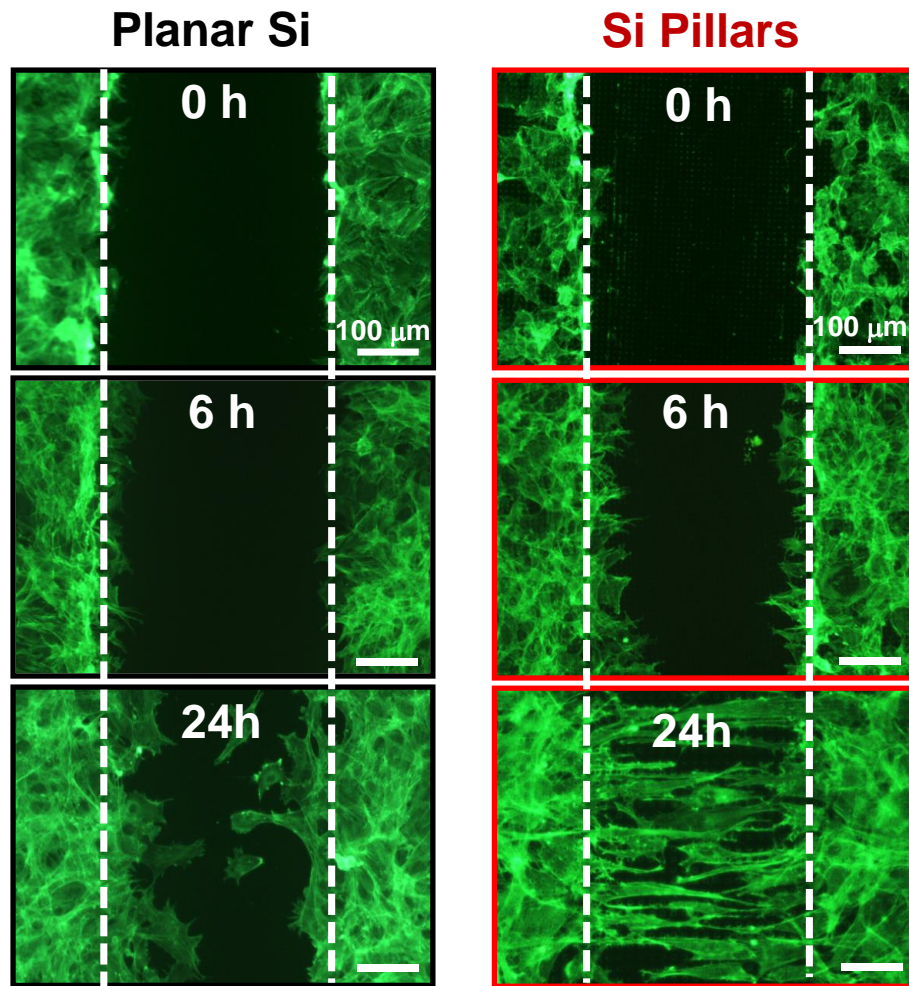


Fig. S6. Fluorescent images demonstrating migration behaviors of MC3T3-E1 cells. These cells are cultured on planar Si (left) and Si pillars (right) after seeded for 0 h, 6 h and 24 h, green: actin cytoskeleton.

Fig. S7.

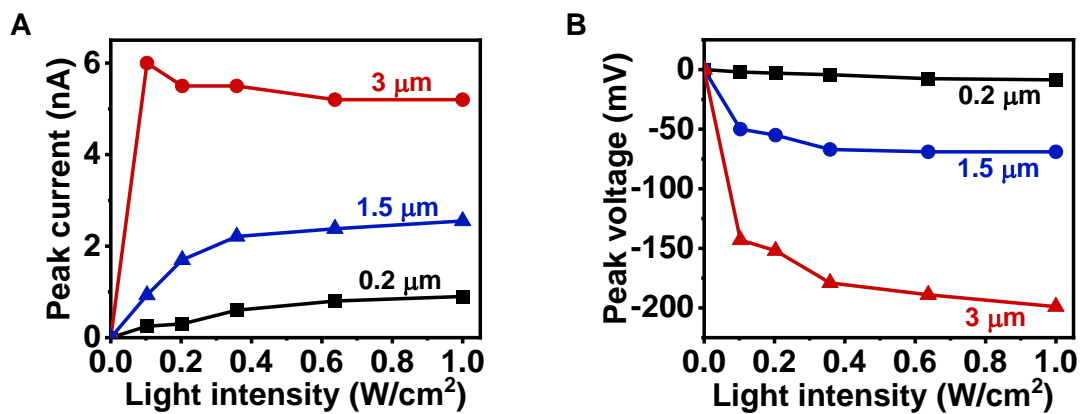


Fig. S7. Optoelectronic properties of Si films with various thicknesses. Measured peak current (A) and peak voltage (B) versus light intensity for Si films with thicknesses of 0.2 μm , 1.5 μm and 3 μm .

Fig. S8.

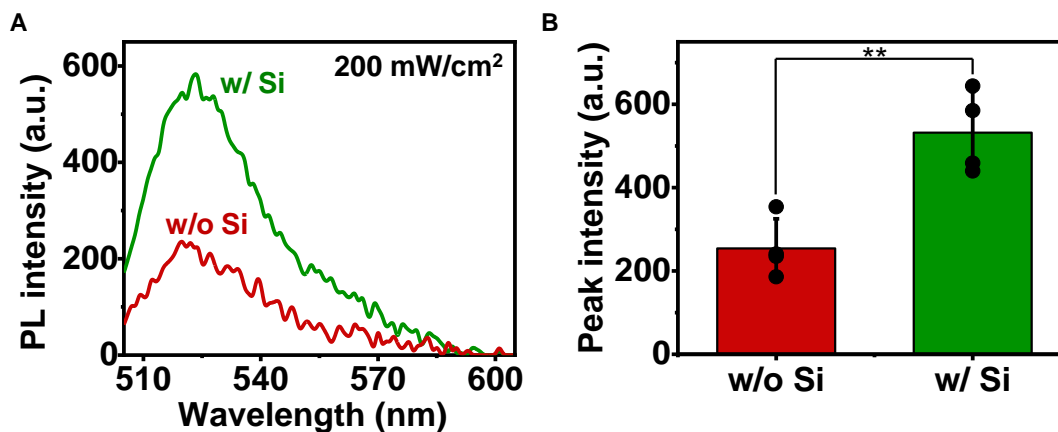


Fig. S8. Photoelectrochemical response of Si films. (A) Recorded photoluminescence (PL) spectra for 2,7-dichloro-dihydro-fluorescein, (DCFH) in PBS solution, under optical illumination (808 nm, power 200 mW/cm², duration 3 mins). The signals indicate the increased level of ROS on Si samples. (B) Statistical results showing peak PL intensity for solutions with and without Si samples. Results are presented as means \pm s.e.m ($n = 4$ samples, ** $P < 0.01$).

Fig. S9.

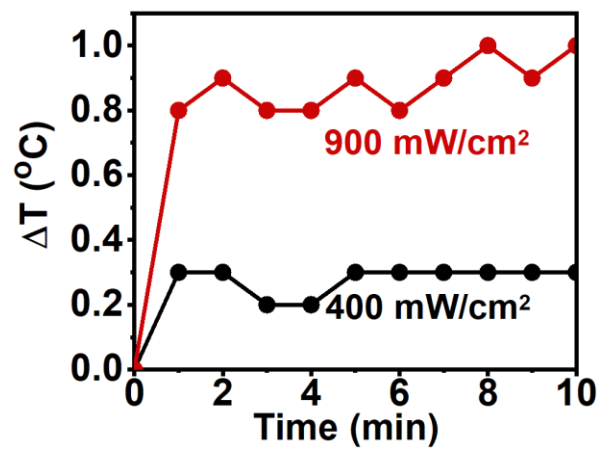


Fig. S9. Photothermal properties of Si films. Measured temperature rise of Si in PBS solution with a thermocouple exposed to 808 nm laser radiation (0.2 Hz, 3 s duration).

Fig. S10.

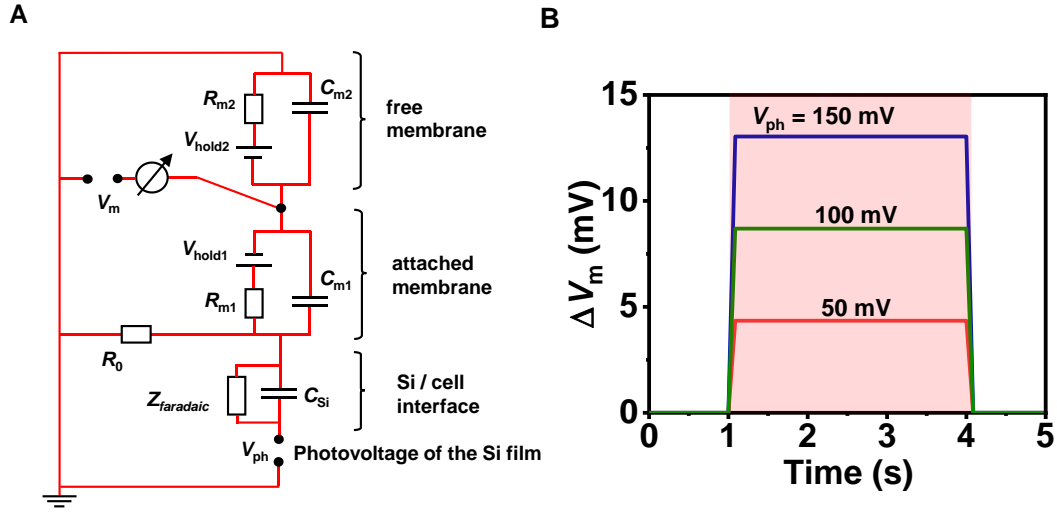


Fig. S10. Numerical simulation of the Si/cell interface. (A) Circuit model established to demonstrate the cellular depolarization by photostimulation. (B) Calculated membrane voltage changes (ΔV_m) responding to different photovoltages (V_{ph}) generated by Si. Here we assume the cell has a hemispheric shape with a spread area of $1500 \mu\text{m}^2$. $R_{m1} = 66.9 \text{ M}\Omega$, $R_{m2} = 33.45 \text{ M}\Omega$, $C_{m1} = 27.3 \text{ pF}$, $C_{m2} = 54.6 \text{ pF}$, $C_{Si} = 70.7 \text{ pF}$ and $Z_{faradaic} = 8 \text{ M}\Omega$. The initial holding potential $V_{hold1} = V_{hold2} = -30 \text{ mV}$.

Fig. S11.

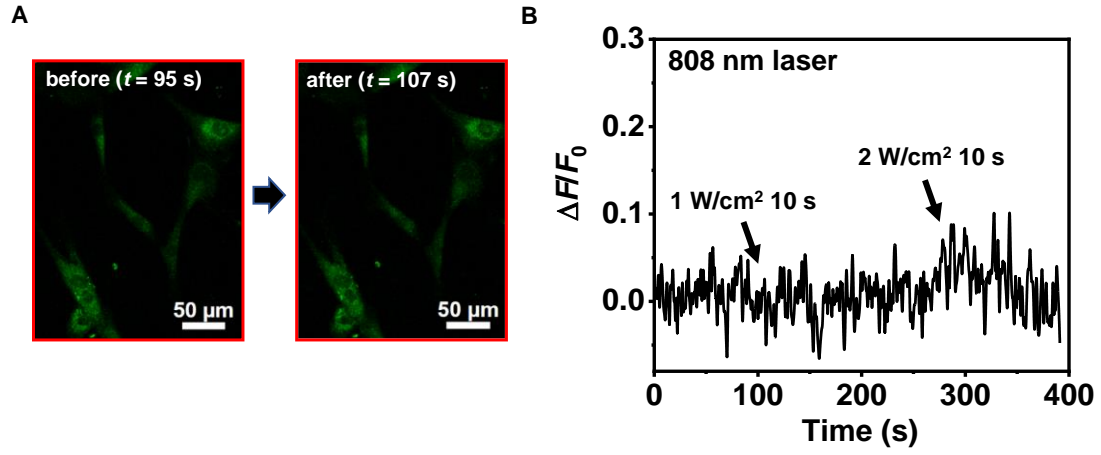


Fig. S11. Calcium activities for hBMSCs on glass. (A) Confocal microscopic images showing of hBMSCs on glass before and after laser stimulation. (B) Intracellular Ca²⁺ flux ($\Delta F/F_0$) measured under illumination with strong radiation intensities. No obvious Ca²⁺ spikes are observed.

Fig. S12.

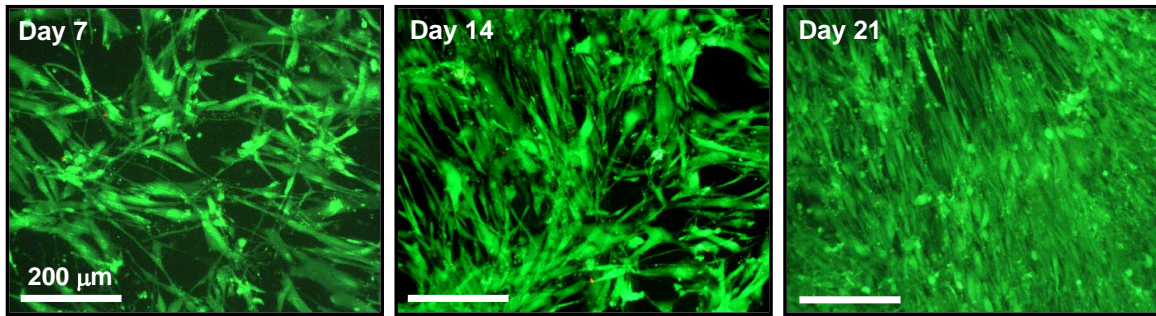


Fig. S12. Phototoxicity characterization. Fluorescent images showing the chronic biocompatibility of Si pillars under 808 nm laser illumination (200 mW/cm², 0.2 Hz, duration 3 s, 20 min every other day), examined by conducting cell live (green) / dead (red) staining tests.

Fig. S13.

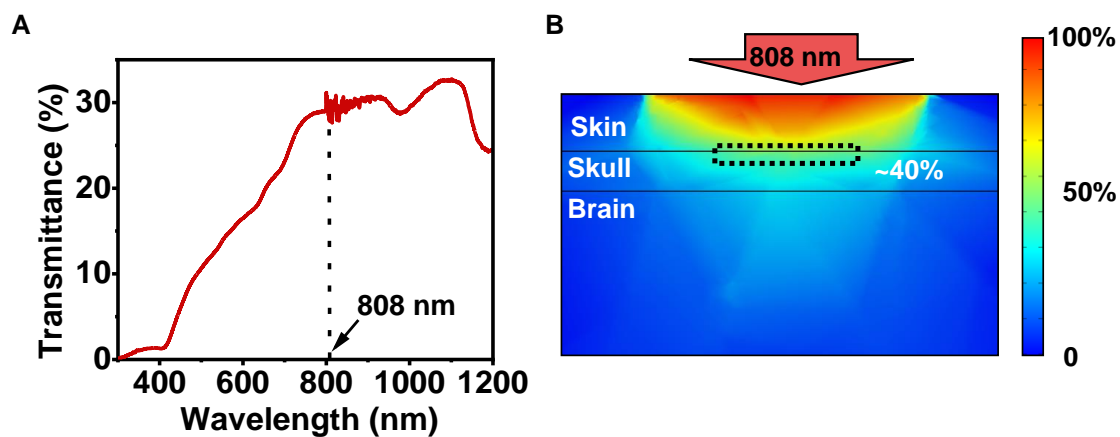


Fig. S13. Optical properties of biological tissues. (A) Measured transmission spectrum of the rat skin tissue (thickness ~2 mm). (B) Simulated light intensity distribution for 808 nm laser incident on the living tissue. The thickness of the skin is 2 mm.

Fig. S14.

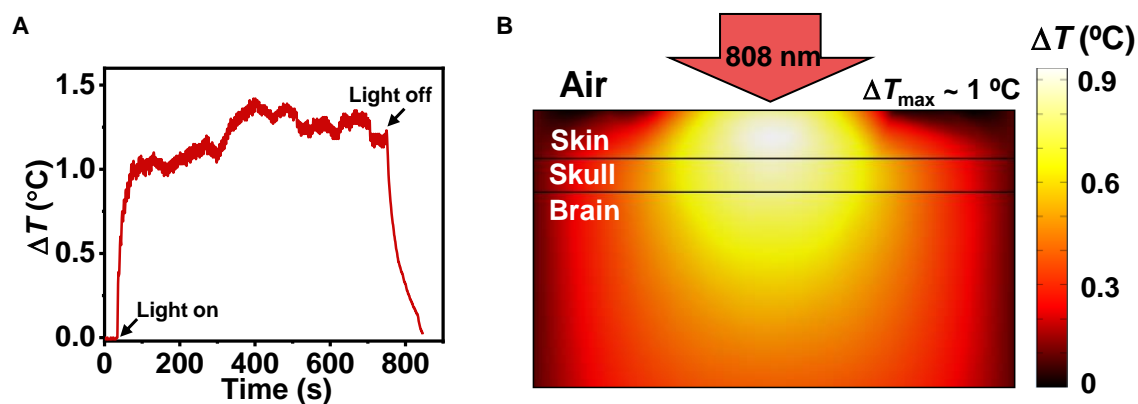


Fig. S14. Photothermal response of biological tissues. (A) Measured temperature rise under rat skin with a thermocouple exposed to $0.8 \text{ W}/\text{cm}^2$, 3s duration 0.2 Hz light radiation. (B) Simulated temperature distribution of tissue samples irradiated with an 808 nm laser at $0.8 \text{ W}/\text{cm}^2$.

Fig. S15.

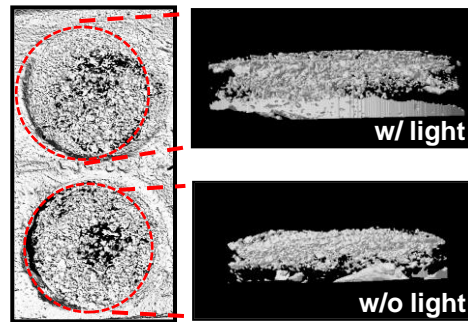


Fig. S15. Micro-CT images showing the radiological analysis of bone samples collected 4 weeks post implantation, (left: top view; right: side view).

Fig. S16.

Blank: without scaffold

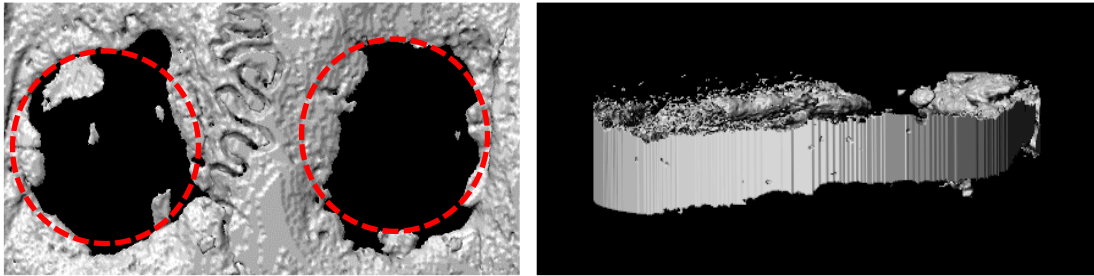


Fig. S16. Micro-CT images showing cranial defects in a rat without 3D scaffolds 8 weeks post surgery. Left: top view; Right: side view.

Fig. S17.

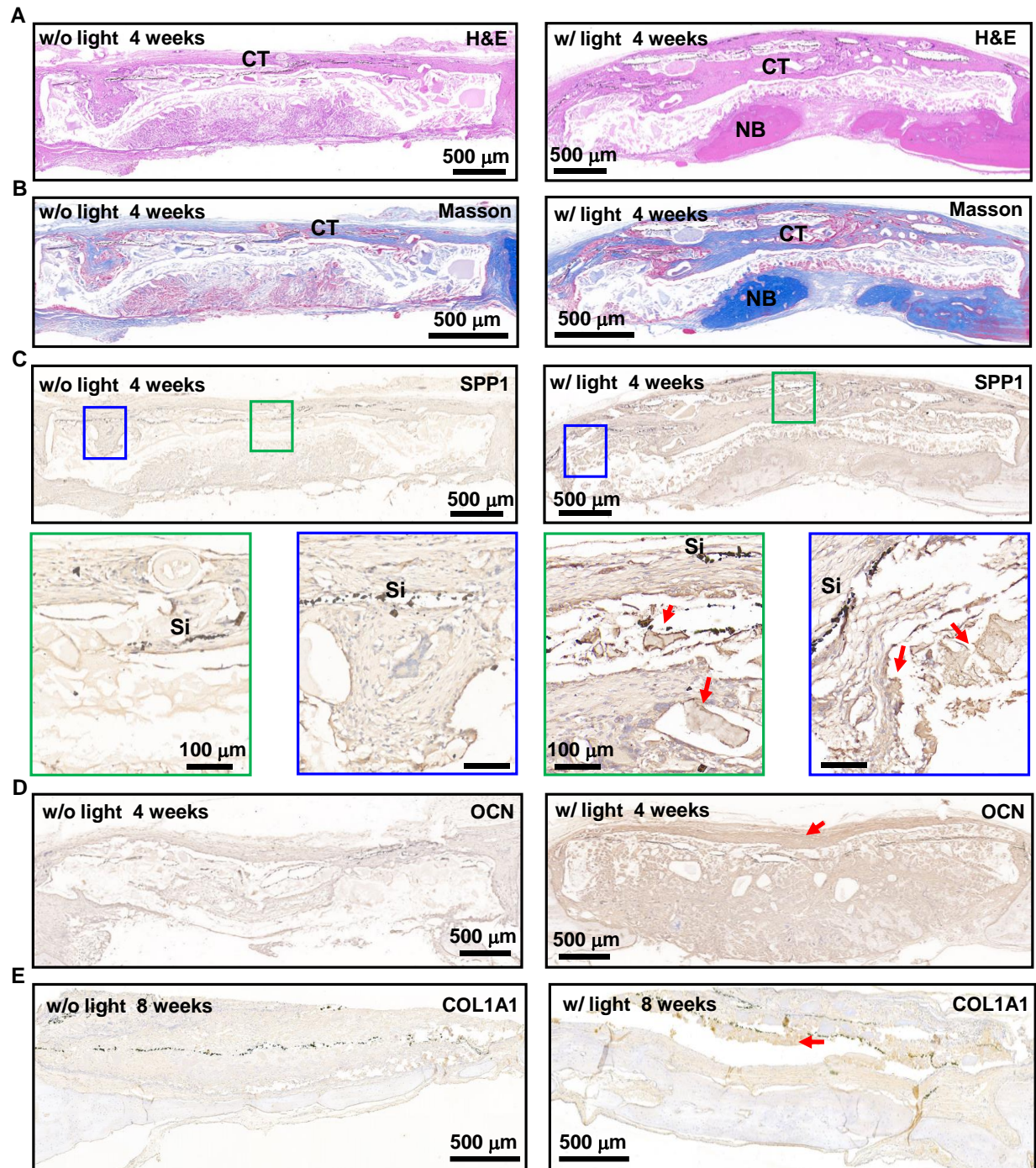


Fig. S17. Histological staining results. (A) H&E staining, (B) Masson staining and immunohistochemical staining of (C) SPP1, (D) OCN and (E) Col1A1 images of regenerated bone tissues with 3D scaffolds 4 weeks and 8 weeks post implantation. NB: newly formed bone, CT: connective tissues.

Fig. S18.

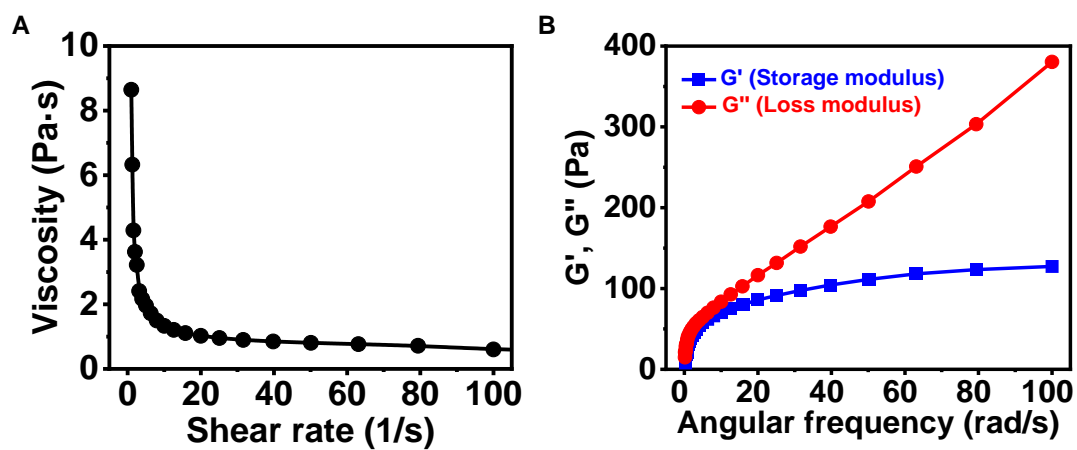


Fig. S18. Rheological properties of the slurry. (A) Measured viscosity versus shear rate for the slurry. (B) Storage modulus G' (blue) and loss modulus G'' (red) versus angular frequency for the slurry. Results are measured at 25 °C.